Postprint of: Saidi T., Palmowski D., Babicz-Kiewlicz S., Welearegay T. G., El Bari N., Ionescu R., Smulko J., Bouchikhi B., Exhaled breath gas sensing using pristine and functionalized WO3 nanowire sensors enhanced by UV-light irradiation, Sensors and Actuators B: Chemical, Vol. 273 (2018), pp. 1719-1729, DOI: 10.1016/j.snb.2018.07.098

Exhaled breath gas sensing using pristine and functionalised WO_3 nanowire sensors enhanced by UV-light irradiation

Tarik Saidi[a, b], Dariusz Palmowski[c], Sylwia Babicz-Kiewlicz[c], Nezha El Bari[b], Tesfalem Geremariam Welearegay[d], Radu Ionescu[e], Janusz Smulko[c], Benachir Bouchikhi[a,*]

[a]*Sensor Electronic & Instrumentation Group, Moulay Ismaïl University, Faculty of Sciences, Department of Physics, B.P. 11201, Zitoune, Meknes, Morocco*

[b]*Biotechnology Agroalimentary and Biomedical Analysis Group, Moulay Ismaïl University, Faculty of Sciences, Department of Biology, B.P. 11201, Zitoune, Meknes, Morocco*

[c]*Department of Metrology and Optoelectronics, Gdańsk University of Technology, Gdańsk, Poland*

[d]*Department of Electronics, Electrical and Automatic Engineering, Rovira i Virgili University, Tarragona 43007, Spain*

[e]*The Ångström Laboratory, Department of Solid State Physics, Uppsala University, 75121 Uppsala, Sweden*

[*]Corresponding author:
Postal address: B.P. 11201, Zitoune 50003 Meknes
Tel: +212 535 53 88 70; Fax: +212 535 53 68 08
benachir.bouchikhi@gmail.com

Abstract

The development of advanced metal-oxide-semiconductor (MOS) sensing technologies for the detection of volatile organic compounds (VOCs) present in the exhaled breath is of great importance for non-invasive, cheap and fast medical diagnostics. Our experimental studies investigate the effects of operating temperature selection and UV-light irradiation on improving the sensitivity of WO_3 nanowire sensors for exhaled breath exposure. Herein, six WO_3 nanowire sensors (both pristine and doped with a range of metal nanoparticles such as Pt, Au, Au/Pt, Ni and Fe) were synthesised via aerosol-assisted chemical vapour deposition (AACVD) and characterised by means of atomic force microscopy (AFM), scanning electron microscopy (SEM), transmission electron microscopy (TEM) and energy dispersive X-ray (EDX-ray). Breath measurements were performed in the dark and under UV-light irradiation at various sensor operating temperatures. The results demonstrate that UV-light irradiation combined with the optimisation of the sensors' operating temperature can greatly enhance the sensors' responses towards breath exposure.

Keywords

WO_3 nanowire sensors, metal nanoparticles, sensitivity enhancement, UV-light irradiation, operating temperature, exhaled breath analysis.

1. Introduction

Exhaled breath is a valuable, non-invasive biological tool available for diagnosing and monitoring medical conditions (Gardner et al., 2000; Adiguzel & Kulah 2015; Lentka et al., 2016; Saidi et al., 2018). Its popularity in medicine can be demonstrated by an increase in papers published in this area. Therefore, the development of advanced and cheap sensors of high sensitivity towards low concentrations of VOCs in the exhaled breath is of paramount importance. In this regard, MOS chemical gas sensors have emerged as a very promising tool for monitoring low concentrations of gaseous compounds (Konvalina & Haick 2014; Welearegay et al., 2016; Zhang et al., 2017), and they represent a low-cost alternative as compared to other available analytical methods (e.g., Gas Chromatography/Mass Spectrometry) that require expensive and bulky equipment.

Tungsten trioxide (WO_3), with a band gap of about 2.8 eV (Yun et al., 2016), is one of the most important n-type MOSs, and it has been extensively used as a gas sensor material for VOC detection (Righettoni et al., 2010; Choi et al., 2014; Kim et al., 2016; Shendage et al., 2017). However, its selectivity and sensitivity are still too low for some applications, such as breath analysis. The selectivity can be partially improved by using a set of sensors with different cross-sensing performances and enhanced by reducing the particle size to a range of 5 to 50 nm (Yamazoe, 1991; Shimizu and Egashira, 1999; Ederth at al., 2006). Alternatively, the sensing potential of WO_3 sensors can be significantly improved by doping the sensing layer with a small amount of metal nanoparticles (NPs), such as platinum, gold, nickel, iron, etc. (Vallejos et al., 2013; Ahsan et al., 2013; Vilic and Llobet 2016). Metal doping

is considered a crucial option for diversifying the selectivity and improving the sensitivity of the sensors. Nevertheless, the sensing performance of the WO_3 sensors must be further optimised to satisfy the requirements for breath analysis applications.

WO_3 NW sensors generally operate at elevated temperatures because the detection mechanisms are based on thermo-activated chemical reactions between the sensing film and the adsorbed VOCs (Bendahan et al., 2007). Variation of the sensor's operating temperature may enhance its sensitivity (Paulsson and Winquist, 1999; Taurino et al., 2002; Ionescu and Llobet 2002; Zhang et al., 2015). Besides, many researchers have proven that WO_3 sensor performance could be influenced by a photocatalytic effect such as UV-light irradiation (Iliev et al., 2010; Giberti et al., 2012; Smulko et al., 2015; Trawka et al., 2016; Gonzalez et al., 2016). The sensitive film of the sensor absorbs the UV-light (Mishra et al., 2004), which provides a further dissociation of the gaseous compounds and the consequent molecule adsorption (Trawka et al., 2016). UV-light irradiation creates a charge transport that increases the density of free electron–hole pairs (Karaduman et al., 2014; Xu et al., 2015). Therefore, it alters the sensing layer. Moreover, the applied UV-light of selected wavelengths can modulate the sensing properties in a different way due to various penetration depths, related to the applied wavelength and morphology of the porous gas sensing layer. Altogether, the response of MOS gas sensors can be successfully modified by UV-light that reduces the necessary heating energy (Park et al., 2013; Espid and Taghipour, 2017).

In our paper, pristine and metal-doped WO_3 NWs were elaborated using aerosol-assisted chemical vapour deposition (AACVD) and characterised by using Atomic Force Microscopy (AFM), Scanning Electron Microscopy (SEM), Transmission Electron Microscopy (TEM) and Energy Dispersive X-ray (EDX-ray). The effects of UV-light irradiation and operating temperature selection were investigated regarding the analysis of exhaled breath.

2. Materials and methods

2.1. Sensor fabrication

AACVD was used to grow WO_3 NWs due to its simplicity and relatively low temperature experimental conditions (Annanouch et al., 2013; Qadri et al., 2016). This method consists of delivering a suitable precursor in the form of an aerosol into the reactor where the substrate is mounted (Stoycheva et al. 2012).

In our study, six different sensors (*i.e.*, pristine WO_3 NWs and the following pool of metal-doped WO_3 NWs: Pt/WO_3; $Au/Pt/WO_3$; Au/WO_3; Ni/WO_3; and Fe/WO_3) were grown using AACVD. Alumina substrates with Pt interdigitated electrodes on the front-side and a Pt meander heater on the back-side were employed as sensing substrates from *CeramTec*© (Marktredwitz, Germany). The substrates were successively cleaned with ethanol, acetone and distilled water and dried with a nitrogen flow before they were placed inside the AACVD reactor.

The layers of WO_3 NWs were prepared using tungsten hexacarbonyl (WC_6O_6) as a precursor according to previous reported procedures (Annanouch et al., 2015; Thamri et al., 2016). The experimental conditions for growing the six sensors are provided in Table 1. After nanomaterial synthesis, the deposited films were annealed in an oven (Carbolite's calcination furnace 1200 °C | BWF) at 500 °C for 180 minutes under a constant flow of 200 mL/min of synthetic air. This step was carried out in order to clean the surface of deposition residues and to stabilise and crystallise the structure of the grown nanomaterials (Stankova et al., 2005; Ng et al., 2015). Otherwise, the morphology and composition of the deposited films were characterised. SEM measurements were performed using a FEI-ESEM Quanta 600 equipment (20 keV), which was coupled to an EDX analyser from *Oxford Instruments*. A TEM analysis of the Nanoparticles' sizes was done by JEOL JEM-1011 equipment with an accelerating energy of

100 keV while the structure of the deposited film was studied with AFM by means of a Keysight 5500 SPM.

AACVD reaction of WC_6O_6 with a mixture of acetone and methanol, inside a hot wall reactor, resulted in the formation of blue-black WO_3 films. Applying the annealing process on these films at 500 ºC yielded yellow layers that indicated fully oxidised WO_3. AFM analysis was used in acoustic mode to assess a topography of the annealed surface of the deposited layers. Figure 1 presents orthogonal 3D images of the AFM topography of pristine and functionalised WO_3 films deposited onto alumina substrate which is scanned within an area of 10 μm². It can be seen that the maximal heights of the pristine WO_3 and Fe/WO_3 NWs were 2.2 μm and 3.4 nm, respectively (Fig. 1.a, Fig. 1.f). However, a significant reduction of surface roughness was achieved by functionalising the sensing surface with metal nanoparticles (except for Fe nanoparticles). Maximal heights of 762 nm, 713 nm, 991 nm and 505 nm for Pt/WO_3 (Fig. 1.b), Au/Pt/WO_3 (Fig. 1.c), Au/WO_3 (Fig. 1.d) and Ni/WO_3 (Fig. 1.e) were obtained, respectively. In all cases, AFM images showed complete coverage of the WO_3 films on the entire substrate surface. It seems that the shape of the grains varied when changing the catalysts. Figure 2.a shows a typical SEM image of the pristine WO_3. It can be seen that the AACVD method at 500 °C produced a layer of thick NWs (about 159 nm), with high density and quite a homogeneous distribution on the entire substrate. In contrast, the films that contain Pt and/or Au Nps exhibited a mixture of randomly distributed nanowires with a diameter ranging between 45 and 57 nm (Fig. 2.b, Fig. 2.c and Fig. 2.d). The layer of Ni/WO_3 showed high density NWs which were randomly distributed (Fig. 3.e). SEM data of Fe/WO_3 also show NWs of various sizes with a diameter ranging between 47 and 126 nm (Fig. 2.f). The AACVD yields a high density of non-aligned nanowires, with a relatively homogeneous distribution containing small pores over the studied surfaces. TEM of the deposited layers for pristine and functionalised WO_3 displayed porous polycrystalline films in thinner structures, approximately as spherical or

cylindrical morphologies (Fig. 3). Nanowires and nanoparticles can be easily observed from the recorded images. They appear well dispersed along the surface of the WO_3 films. The grain diameters of the studied metal Nps were about 11 nm for Pt Nps (Fig. 3.b), 4.63 nm for the alloy of Au/Pt Nps (Fig. 3.c), 3.97 nm for Au Nps (Fig. 3.d), 39 nm for Ni Nps (Fig. 3.e) and 8.22 nm for Fe Nps (Fig. 3.f). The results show that the set of the investigated sensors was characterised by their high surface-to-volume ratio, which provides more surface area for both chemical and physical interactions and therefore secures better sensitivity. The EDX spectrum (Fig. 4) showed tungsten, oxygen and alumina (from the substrate) as the major peaks, and also revealed the presence of metal nanoparticles on the surface of the sensing nanomaterials. The percentages of metal nanostructures on the sensing films varied between 1% and 2% except for Pt Nps where it is found within 6% to 7% due to presence of platinum connectors to the substrate.

2.2. Measurement set-up and conditions

The main part of the presented experimental studies required a collection of exhaled breath samples. To avoid any eventual artefacts, the breath samples were taken from the same individual (non-smoker, adult man) using Tedlar® bags before any food or beverage consumption. For this, the person took a deep breath, and breathed normally into the collection bag before empting his lungs. The breath sample was immediately transferred from the collection bag into the gas chamber where the sensors were placed. This was done by pumping the contents of each filled bag at a constant flow rate of 100 mL/min.

The experiments began by starting a flow of current through the sensors' heaters, corresponding to the selected temperature, for 1000 s. Next, the sensors were exposed to the collected breath sample for 40 min, and ended with the next 80 min of recovery under laboratory air using the same flow rate of 100 mL/min. An exposure of the sensors' to the exhaled breath was done both in dark and under UV-light irradiation. The sensors' conductance was continuously recorded at

158 a sampling rate of 1 Hz using an NI USB-6212 data acquisition board from *National*
159 *Instruments* (Texas, USA). The sensors' conductance was determine by measuring the DC
160 voltage across the sensor as part of a voltage divider with another resistor connected in series
161 and supplied by a DC voltage of 5 V. Figure 5 shows the circuit of the electrical current control
162 unit for the heaters of three sensors. This unit was repeated to supply DC current for the next
163 three heaters. The operating temperature was controlled by choosing the resistances of the
164 heaters (RHn, n = 1 … 6) with a selected current, adjusted by a potentiometer (P).
165 The experiment was performed using an array of six independent sensors in the dark and under
166 UV-light irradiation emitted by six OSV4YL5451B type diodes from *Opto-Supply*, China. Each
167 diode was mounted above the sensor at the same distance, and the optical power irradiating the
168 gas sensing layer was similar for each sensor.

169 The relative humidity and temperature inside the gas chamber was monitored during the
170 experiment with a HIH 4000-002 humidity sensor from *Honeywell*, USA, and a LM35DZ
171 temperature sensor from *Texas Instruments*, USA. The stability of the relative humidity
172 (28% ± 5%) and temperature (40°C ± 1°C) were recorded.

173 ## 3. Results and discussion

174 Firstly, an experimental study was performed to find the most suitable operating temperatures
175 of the sensors that secured the best responses to exhaled breath samples. It was found that each
176 sensor has a range of operating temperatures, usually between 90ºC and 120ºC for pristine WO_3,
177 Pt/WO_3 and $Au/Pt/WO_3$ sensors (Subset #1), and between 140°C and 200°C for Au/WO_3,
178 Ni/WO_3 and Fe/WO_3 sensors (Subset #2). We selected temperature ranges to include the
179 optimal operating temperature for both sensor batches when exposed to breath samples.

180 Figure 6 shows the sensors' responses towards two successive breath exposures in the dark
181 (blue curves) and under UV-light irradiation (red curves); the sensors from Subset #1 operated

at 100 ºC (Fig. 6.a, Fig. 6.b, Fig. 6.c), and the sensors from Subset #2 at 160 °C (Fig. 6.d, Fig. 6.e and Fig. 6.f). Importantly, it can be seen that the sensors' responses became relatively more intense under UV-light irradiation than in the dark. This effect can be measured by a quotient Q of two conductances:

$$Q = \frac{G_{\mathrm{F_{UV}}}}{G_{F_{dark}}} \times 100\% \quad (1)$$

where:

- $G_{\mathrm{F\_UV}}$ – conductance observed after breath exposure under UV-light at the final stage of the experiment,
- $G_{\mathrm{F\_dark}}$ – conductance observed after breath exposure in the dark at the final stage of the experiment.

The quotient Q reached at least 150%. For the pristine WO_3 NW sensor, it reached Q = 323%. This result is associated with the photocatalytic reactions taking place in the sensing film and with decomposition of the breath VOCs that are then adsorbed by the sensing material (Trawka et al., 2016). When the photons' energy overtakes the energy band gap E_g of the semiconductor, a generated electron (e^-) in the valence band is excited into the conduction band, leaving a positive hole (h^+) in the valence band (Wu et al., 2015). The energy gap of WO_3 is $E_g \approx 2.8$ eV, whereas the UV LEDs' wavelength is 394 nm, corresponding to a photon energy of 3.15 eV. As a photon's energy emitted from the UV LEDs is higher than the energy gap for WO_3 material, the sensor's conductance under UV-light irradiation should depend on the interband transitions (Giberti et al., 2012).

When the sensors operated under UV-light irradiation, their responses were repeatable and their recovery time was relatively short (Fig. 6). When the sensors operated under dark conditions, their responses were much longer and exceeded the observation time. We can claim that the use

of UV-light irradiation accelerated the desorption rate of the VOCs adsorbed by the sensing film before we switched to only the laboratory air. At the same time, UV-light quickened the saturation of the investigated sensors when exposed to VOCs.

Figure 7 displays the responses to breath exposure of three investigated sensors operating at selected temperatures. The presented data proves that under UV-light irradiation, the sensors provide more repeatable responses and with more intense relative changes of conductance as compared to their operation under dark conditions. This effect may be explained by intensified desorption in the presence of UV light which accelerates cleansing of the sensors after breath exposure. We have noticed that an increase of the sensor's operating temperature quickened its response but decreased its relative changes of conductance. Thus, for the pristine WO_3 NW sensor, the UV/dark ratio (*see* Eq. 1) increased from 342% at 90 °C to 419% at 110 °C (when the sensor had not reached saturation during the experiment). At an operating temperature of 120 °C, the sensor response in the dark (blue curve) was more intense than at lower temperatures, and therefore the UV/dark ratio of conductances decreased to 212% (Fig. 7.a, Fig. 7.b and Fig. 7.c). In the case of the Au/Pt/WO_3 sensor, an operating temperature of 90 °C was too low to observe saturation or full recovery during the time of the experiment. The sensor started to saturate at a temperature of 110 ºC both in the dark and under UV-light operation. UV-light irradiation assured a faster response, requiring only a few minutes, when compared to dark conditions, requiring about 30 min (Fig. 7.d, Fig. 7.e). For this sensor, again, the operating temperature of 120 ºC assured more intense relative changes of conductance under dark conditions than at lower temperatures (Fig. 7.f). This is also observed for the Au/WO_3 sensor at different operating temperatures. This sensor (Subset #2), showed that at an operating temperature of 140 °C, saturation cannot be achieved in the dark nor under UV-light (Fig. 7.g). Full saturation at an operating temperature of 180°C is reached after about 30 min of breath exposure in the dark and after about 15 min under UV-light (Fig. 7.h). As a consequence,

the coefficient *Q* decreased from 333% at 180 ºC to 181% at 200 °C (Fig. 7.i). These results suggest that the presence of metal NPs on WO_3 NW surfaces could seriously improve the sensor's sensitivity to exhaled breath exposure, while reducing its optimal operating temperature.

Based on the time of response, operating temperature of the investigated sensors and relative change of DC resistance, we may determine their sensitivity to the exhaled breath. Sensitivity *S* can be defined as a relative change of conductance G_F measured at the end of observation time (final conductance) in the ambient atmosphere of the exhaled breath and under dark conditions or UV-light irradiation (by using the index "dark or UV") and referenced to *G* measured in the ambient atmosphere of laboratory air:

$$S = \frac{G_{\mathrm{F\ (dark\ or\ UV)}} - G_{\mathrm{0\ (dark\ or\ UV)}}}{G_{(dark\ or\ UV)}} \times 100\% \quad (2)$$

All six sensors exhibited greater sensitivity when measured under UV-light irradiation at the investigated operating temperatures. Subset #1 of the sensors (pristine WO_3, Pt/WO_3 and Au/Pt/WO_3) reached higher sensitivities towards breath exposures at 100 °C both in the dark and under UV-light irradiation (Fig. 8.a, Fig. 8.b), which drastically decreased at 110 ºC and further at 120 °C under UV-light irradiation. In the case of the sensors from Subset #2 (Au/WO_3, Ni/WO_3 and Fe/WO_3), their sensitivity changed slightly at the considered operating temperatures and in the dark (Fig. 8.c), while under UV-light irradiation, the changes were much more intense and the greatest sensitivity was observed at 160 ºC (Fig. 8.d). The most significant difference between the sensitivity in the dark and under UV-light irradiation was found for the Au/WO_3 sensor, which increased from 88.9 % to 216.9% at 160 °C.

The reported results mean that a proper combination of the sensors' heating and UV-irradiation may play a crucial role in enhancing MOS WO_3 sensors' sensitivity towards the detection of

the VOC's in the exhaled breath. Their functionalisation by metal-doped nanoparticles is also important to determine the sensors' optimal operating temperature, together with the sensors' sensitivity and selectivity.

4. Conclusions

Our experimental study presents the first ever report of UV-irradiation combined with a selection of the sensors' operating temperatures to enhance exhaled breath detection by WO_3 NW sensors decorated by selected metal dopants. The study was performed on both pristine and NP-doped WO_3 NWs grown by AACVD on alumina substrates and characterised by AFM, SEM, TEM and EDX-ray. All sensors clearly responded to the exhaled breath, both in the dark and under UV-light irradiation. In addition, their responses were repeatable and determined by their operating temperatures. The experimental results revealed that the most sensitive sensor towards the exhaled breath samples was the Au-doped WO_3 NWs operating at 160 °C. It reached a sensitivity as high as $S = 216.9\%$ under UV-light irradiation. These promising results may be a way for further development of low-cost, low-power consumption and highly sensitive gas sensors for medical applications.

Acknowledgments

We would like to thank Moulay Ismaïl University for financial support of the project "Research support". This work has been funded in part by TROPSENSE under the H2020-MSCA-RISE-2014 project, grant agreement number: 645758.

References

Adiguzel, Y., & Kulah, H. (2015). Breath sensors for lung cancer diagnosis. Biosensors and Bioelectronics, 65, 121-138.

Ahsan, M., Ahmad, M. Z., Tesfamichael, T., Bell, J., & Yarlagadda, P. K. (2013). Ethanol sensitivity of thermally evaporated nanostructured WO_3 thin films doped and implanted with Fe. In Applied Mechanics and Materials (Vol. 333, pp. 1938-1945). Trans Tech Publications.

Annanouch, F. E., Gràcia, I., Figueras, E., Llobet, E., Cané, C., & Vallejos, S. (2015). Localized aerosol-assisted CVD of nanomaterials for the fabrication of monolithic gas sensor microarrays. Sensors and Actuators B: Chemical, 216, 374-383.

Annanouch, F. E., Vallejos, S., Stoycheva, T., Blackman, C., & Llobet, E. (2013). Aerosol assisted chemical vapour deposition of gas-sensitive nanomaterials. Thin Solid Films, 548, 703-709.

Bendahan, M., Guerin, J., Boulmani, R., & Aguir, K. (2007). WO_3 sensor response according to operating temperature: experiment and modeling. Sensors and Actuators B: Chemical, 124(1), 24-29.

Choi, S. J., Fuchs, F., Demadrille, R., Grévin, B., Jang, B. H., Lee, S. J., & Kim, I. D. (2014). Fast responding exhaled-breath sensors using WO_3 hemitubes functionalized by graphene-based electronic sensitizers for diagnosis of diseases. ACS Applied Materials & Interfaces, 6(12), 9061-9070.

Espid, E., & Taghipour, F. (2017). Development of highly sensitive ZnO/In_2O_3 composite gas sensor activated by UV-LED. Sensors and Actuators B: Chemical, 241, 828-839.

Gardner, J. W., Shin, H. W., & Hines, E. L. (2000). An electronic nose system to diagnose illness. Sensors and Actuators B: Chemical, 70(1), 19-24.

Giberti, A., Malagù, C., & Guidi, V. (2012). WO_3 sensing properties enhanced by UV illumination: an evidence of surface effect. Sensors and Actuators B: Chemical, 165(1), 59-61.

Gonzalez, O., Welearegay, T., Llobet, E., & Vilanova, X. (2016). Pulsed UV Light Activated Gas Sensing in Tungsten Oxide Nanowires. Procedia Engineering, 168, 351-354.

Iliev, V., Tomova, D., Rakovsky, S., Eliyas, A., & Puma, G. L. (2010). Enhancement of photocatalytic oxidation of oxalic acid by gold modified WO_3/TiO_2 photocatalysts under UV and visible light irradiation. Journal of Molecular Catalysis A: Chemical, 327(1), 51-57.

Ionescu, R., & Llobet, E. (2002). Wavelet transform-based fast feature extraction from temperature modulated semiconductor gas sensors. Sensors and Actuators B: Chemical, 81(2), 289-295.

Karaduman, I., Yıldız, D. E., Sincar, M. M., & Acar, S. (2014). UV light activated gas sensor for NO_2 detection. Materials Science in Semiconductor Processing, 28, 43-47.

Konvalina, G., & Haick, H. (2014). Sensors for breath testing: from nanomaterials to comprehensive disease detection. Acc. Chem. Res, 47(1), 66-76.

Kim, S. J., Choi, S. J., Jang, J. S., Kim, N. H., Hakim, M., Tuller, H. L., & Kim, I. D. (2016). Mesoporous WO_3 nanofibers with protein-templated nanoscale catalysts for detection of trace biomarkers in exhaled breath. ACS nano, 10(6), 5891-5899.

Lentka, Ł., Kotarski, M., Smulko, J., Cindemir, U., Topalian, Z., Granqvist, C. G., Raul Calavia., & Ionescu, R. (2016). Fluctuation-enhanced sensing with organically functionalized gold nanoparticle gas sensors targeting biomedical applications. Talanta, 160, 9-14.

Mishra, S., Ghanshyam, C., Ram, N., Bajpai, R. P., & Bedi, R. K. (2004). Detection mechanism of metal oxide gas sensor under UV radiation. Sensors and Actuators B: Chemical, 97(2), 387-390.

Ng, C. Y., Razak, K. A., & Lockman, Z. (2015). Effect of annealing temperature on anodized nanoporous WO_3. Journal of Porous Materials, 22(2), 537-544.

Park, S., An, S., Ko, H., Lee, S., & Lee, C. (2013). Synthesis, structure, and UV-enhanced gas sensing properties of Au-functionalized ZnS nanowires. Sensors and Actuators B: Chemical, 188, 1270-1276.

Paulsson, N., Larsson, E., & Winquist, F. (2000). Extraction and selection of parameters for evaluation of breath alcohol measurement with an electronic nose. Sensors and Actuators A: Physical, 84(3), 187-197.

Paulsson, N., & Winquist, F. (1999). Analysis of breath alcohol with a multisensor array: instrumental setup, characterization and evaluation. Forensic science international, 105(2), 95-114.

Qadri, M. U., Annanouch, F. E., Aguiló, M., Díaz, F., Borull, J. F., Pujol, M. C., & Llobet, E. (2016). Metal Decorated WO_3 Nanoneedles Fabricated by Aerosol Assisted Chemical Vapor Deposition for Optical Gas Sensing. Journal of Nanoscience and Nanotechnology, 16(9), 10125-10132.

Righettoni, M., Tricoli, A., & Pratsinis, S. E. (2010). Si: WO_3 sensors for highly selective detection of acetone for easy diagnosis of diabetes by breath analysis. Analytical chemistry, 82(9), 3581-3587.

Saidi, T., Zaim, O., Moufid, M., El Bari, N., Ionescu, R., & Bouchikhi, B. (2018). Exhaled breath analysis using electronic nose and gas chromatography-mass spectrometry for non-invasive diagnosis of chronic kidney disease, diabetes mellitus and healthy subjects. Sensors and Actuators B: Chemical, 257, 178-188.

Shendage, S. S., Patil, V. L., Vanalakar, S. A., Patil, S. P., Harale, N. S., Bhosale, J. L., ... & Patil, P. S. (2017). Sensitive and selective NO_2 gas sensor based on WO_3 nanoplates. Sensors and Actuators B: Chemical, 240, 426-433.

Shimizu, Y., & Egashira, M. (1999). Basic aspects and challenges of semiconductor gas sensors. Mrs Bulletin, 24(6), 18-24.

Ederth, J., Smulko, J. M., Kish, L. B., Heszler, P., & Granqvist, C. G. (2006). Comparison of classical and fluctuation-enhanced gas sensing with Pd_xWO_3 nanoparticle films. Sensors and Actuators B: Chemical, 113(1), 310-315.

Smulko, J. M., Trawka, M., Granqvist, C. G., Ionescu, R., Annanouch, F., Llobet, E., & Kish, L. B. (2015). New approaches for improving selectivity and sensitivity of resistive gas sensors: a review. Sensor Review, 35(4), 340-347.

Stankova, M., Vilanova, X., Llobet, E., Calderer, J., Bittencourt, C., Pireaux, J. J., & Correig, X. (2005). Influence of the annealing and operating temperatures on the gas-sensing properties of RF sputtered WO_3 thin-film sensors. Sensors and Actuators B: Chemical, 105(2), 271-277.

Stoycheva, T., Vallejosa, S., Blackmanb, C., Monizb S. J. A., Caldererc J., et al. (2012) Important considerations for effective gas sensors based on metal oxidenanoneedles films. Sensors and Actuators B 161: 406-413.

Stoycheva, T., Annanouch, F. E., Gràcia, I., Llobet, E., Blackman, C., Correig, X., & Vallejos, S. (2014). Micromachined gas sensors based on tungsten oxide nanoneedles directly integrated via aerosol assisted CVD. Sensors and Actuators B: Chemical, 198, 210-218.

Taurino, A., Capone, S., Distante, C., Epifani, M., Rella, R., & Siciliano, P. (2002). Recognition of olive oils by means of an integrated sol–gel SnO_2 electronic nose. Thin Solid Films, 418(1), 59-65.

Thamri, A., Baccar, H., Annanouch, F. E., Llobet, E., & Abdelghani, A. (2016). Methanol, Ethanol and Acetone Sensing Using AACVD-grown Tungsten Oxide Nanoneedles. J Nanomed Nanotechnol, 7(380), 2.

Trawka, M., Smulko, J., Hasse, L., Granqvist, C. G., Annanouch, F. E., & Ionescu, R. (2016). Fluctuation enhanced gas sensing with WO_3-based nanoparticle gas sensors modulated by UV light at selected wavelengths. Sensors and Actuators B: Chemical, 234, 453-461.

Vallejos, S., Umek, P., Stoycheva, T., Annanouch, F., Llobet, E., Correig, X., ... & Blackman, C. (2013). Single-Step Deposition of Au-and Pt-Nanoparticle-Functionalized Tungsten Oxide Nanoneedles Synthesized Via Aerosol-Assisted CVD, and Used for Fabrication of Selective Gas Microsensor Arrays. Advanced Functional Materials, 23(10), 1313-1322.

Vilic, T., & Llobet, E. (2016). Nickel Doped WO_3 Nanoneedles Deposited by a Single Step AACVD for Gas Sensing Applications. Procedia Engineering, 168, 206-210.

Welearegay, T. G., Gualdrón, O. E., Jaimes, A. L., Cáceres, J. M., Pugliese, G., Cindemir, U., ... & Ionescu, R. (2016). Ultrapure Organically Modified Gold Nanoparticles for Breath Analysis. Procedia Engineering, 168, 133-136.

Wu, W., Jiang, C., & Roy, V. A. (2015). Recent progress in magnetic iron oxide–semiconductor composite nanomaterials as promising photocatalysts. Nanoscale, 7(1), 38-58.

Xu, S., Sun, F., Yang, S., Pan, Z., Long, J., & Gu, F. (2015). Fabrication of SnO_2-Reduced Graphite Oxide Monolayer-Ordered Porous Film Gas Sensor with Tunable Sensitivity through Ultra-Violet Light Irradiation. Scientific reports, 5, 1-8.

Yamazoe, N. (1991). New approaches for improving semiconductor gas sensors. Sensors and Actuators B: Chemical, 5(1-4), 7-19.

Yu-De, W., Zhan-Xian, C., Yan-Feng, L., Zhen-Lai, Z., & Xing-Hui, W. (2001). Electrical and gas-sensing properties of WO_3 semiconductor material. Solid-State Electronics, 45(5), 639-644.

Yun, G., Balamurugan, M., Kim, H. S., Ahn, K. S., & Kang, S. H. (2016). Role of WO_3 layers electrodeposited on SnO_2 inverse opal skeletons in photoelectrochemical water splitting. The Journal of Physical Chemistry C, 120(11), 5906-5915.

Zhang, G., & Xie, C. (2015). A novel method in the gas identification by using WO_3 gas sensor based on the temperature-programmed technique. Sensors and Actuators B: Chemical, 206, 220-229.

Zhang, J., Qin, Z., Zeng, D., & Xie, C. (2017). Metal-oxide-semiconductor based gas sensors: screening, preparation, and integration. Physical Chemistry Chemical Physics, 19(9), 6313-6329.

Smulko, J. M., & Kish, L. B. (2004). Higher-order statistics for fluctuation-enhanced gas-sensing. Sensors and Materials, 16(6), 291-299.

Highlights

- AACVD was carried out to produce pristine and differently functionalised WO_3
- The grown sensors were characterised with AFM, SEM, TEM and EDX-ray
- UV-light irradiation enhanced the sensors' responses towards breath exposure
- The most sensitive sensor for breath was the Au-doped WO_3 and operating at 160 °C

Figure 1 AFM topographies of the sensors' surfaces of: **(a)** pristine WO_3; **(b)** Pt/WO_3; **(c)** $Au/Pt/WO_3$; **(d)** Au/WO_3; **(e)** Ni/WO_3; **(f)** Fe/WO_3.

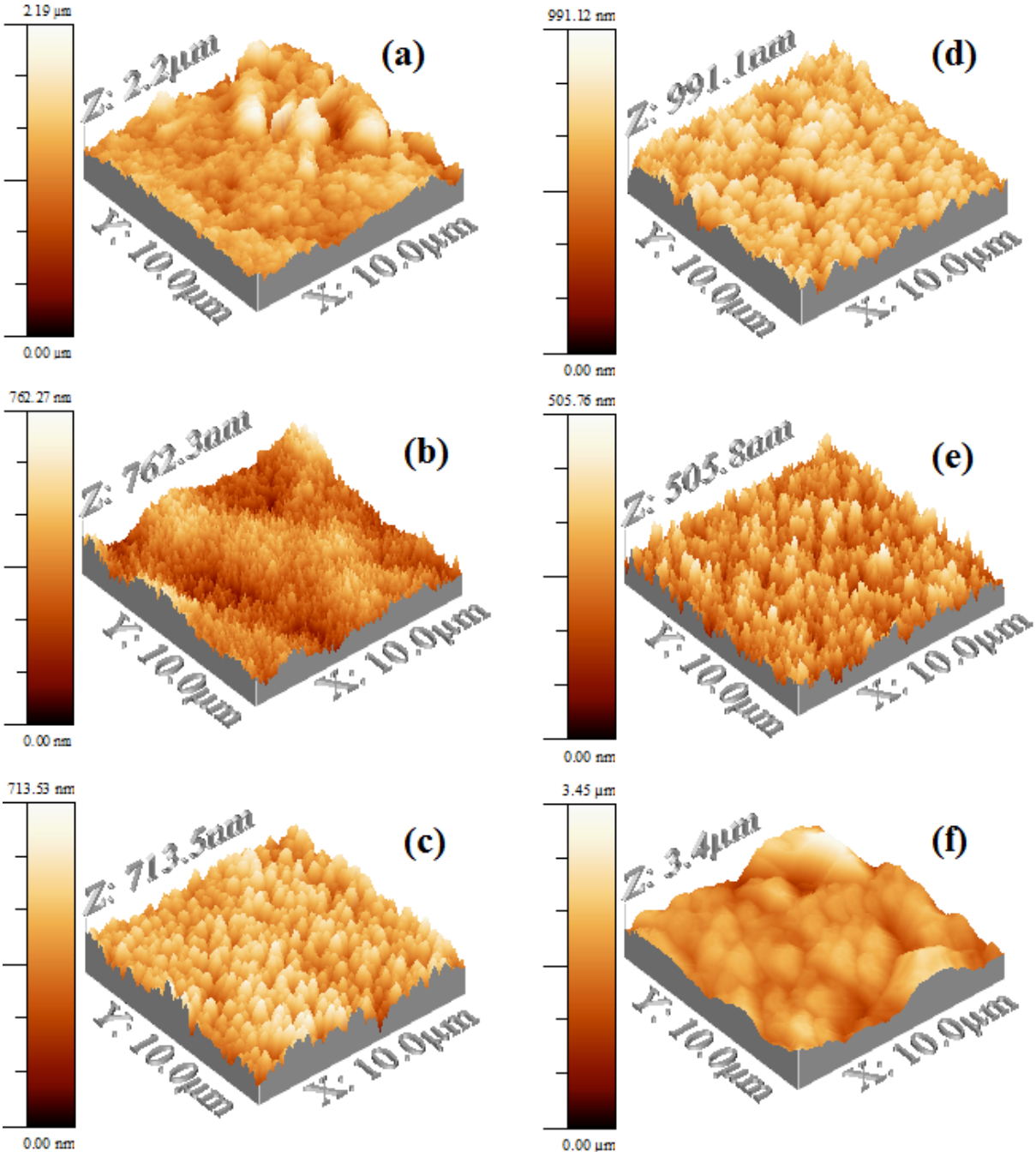

Figure 2 Typical SEM images of sensing areas of: **(a)** pristine WO_3; **(b)** Pt/WO_3; **(c)** Au/Pt/WO_3; **(d)** Au/WO_3; **(e)** Ni/WO_3; **(f)** Fe/WO_3.

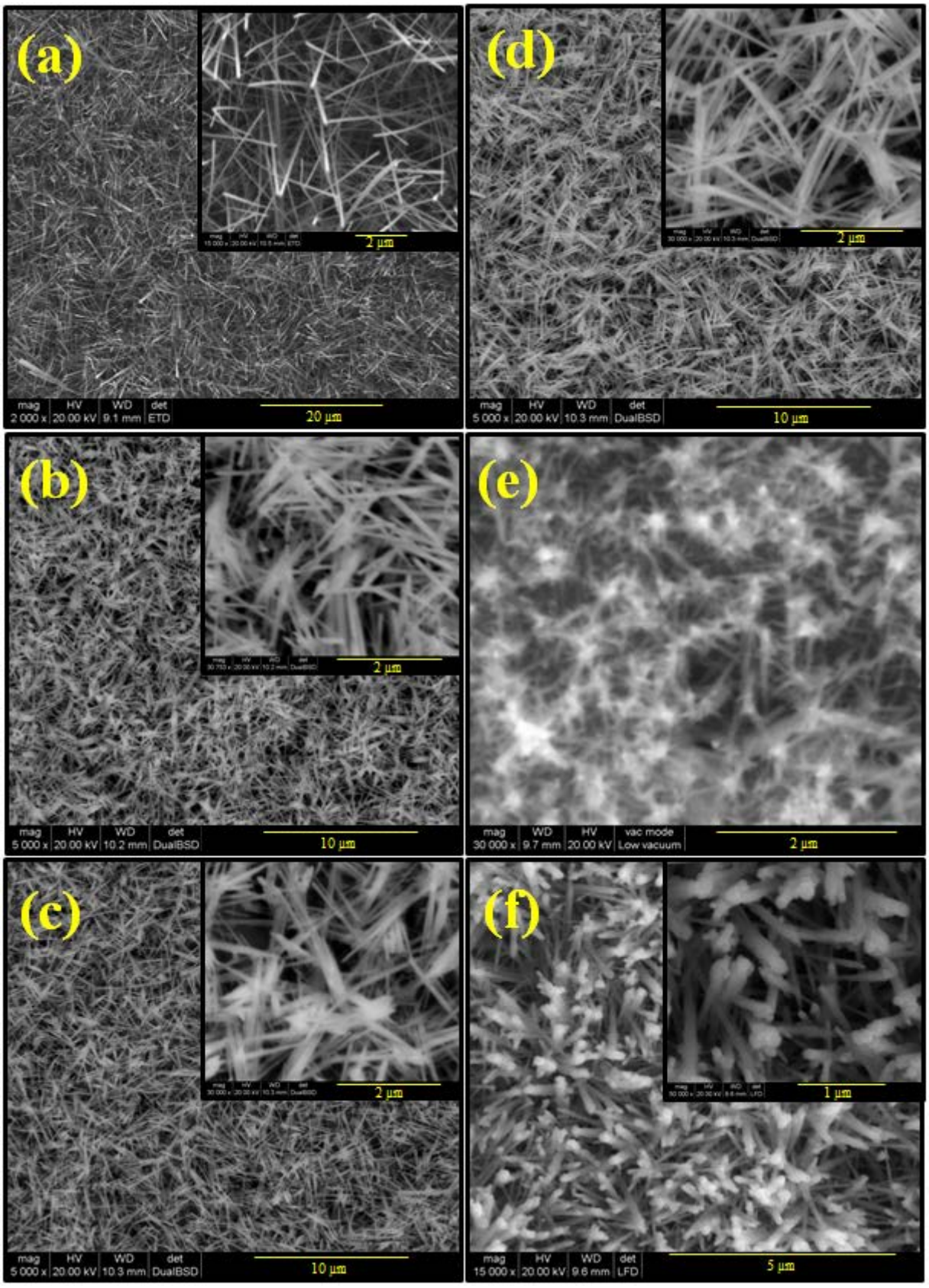

Figure 3 TEM images of the sensitive films of: **(a)** pristine WO_3; **(b)** Pt/WO_3; **(c)** $Au/Pt/WO_3$; **(d)** Au/WO_3; **(e)** Ni/WO_3; **(f)** Fe/WO_3.

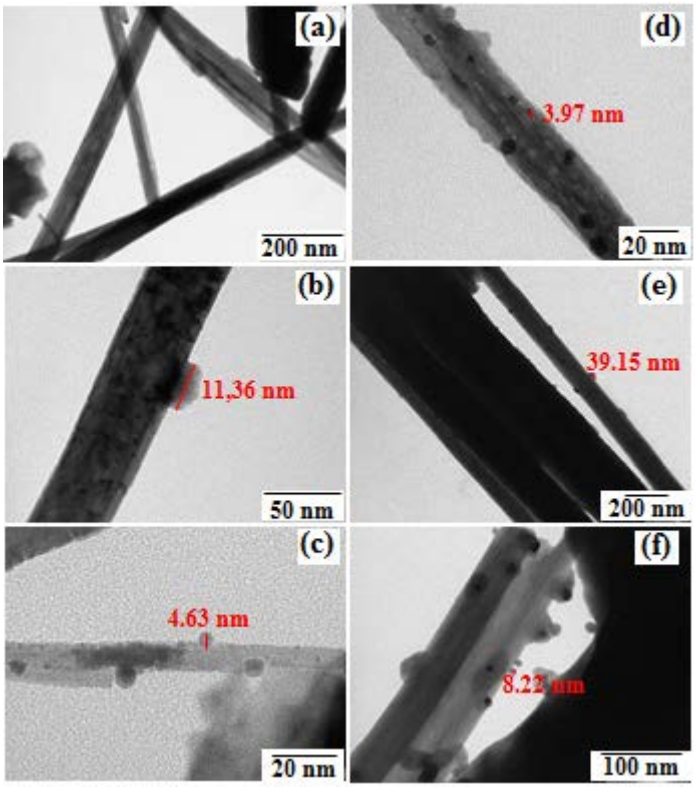

Figure 4 EDX-ray spectrum of the six sensors: **(a)** pristine WO_3; **(b)** Pt/WO_3; **(c)** $Au/Pt/WO_3$; **(d)** Au/WO_3; **(e)** Ni/WO_3; **(f)** Fe/WO_3.

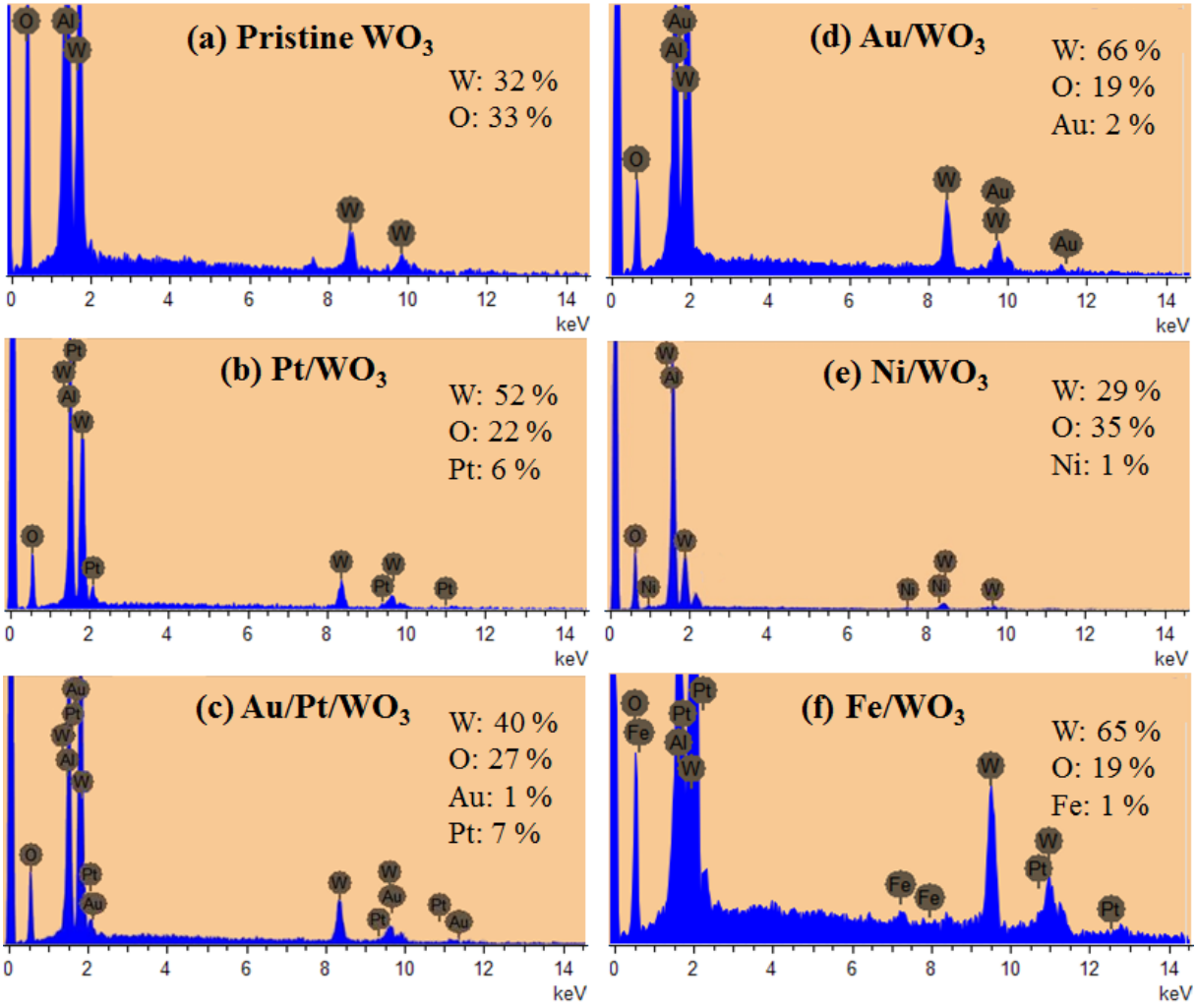

Figure 5 Electronic conditioning circuit for monitoring the current of three sensors' heaters connected in series.

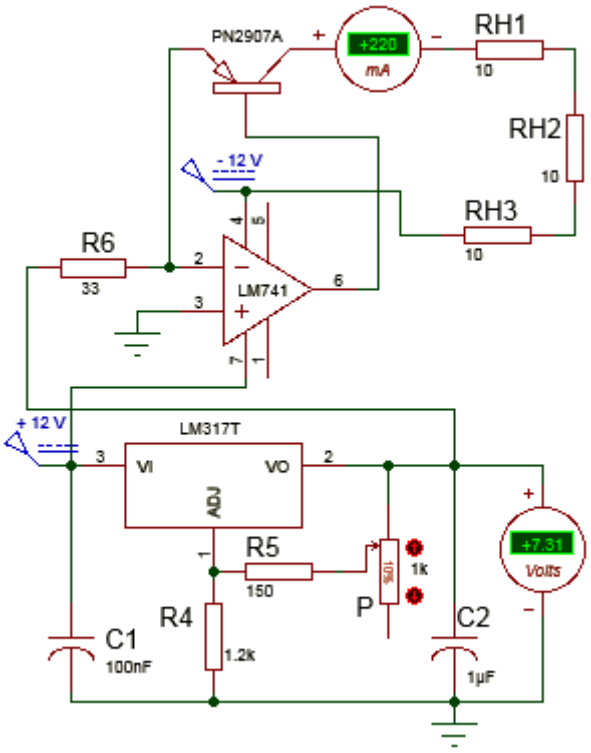

Figure 6 Sensors responses towards two repeated breath exposures in the dark (blue curves) and under UV-light illumination (red curves) for: **(a)** Pristine WO_3; **(b)** Pt/WO_3; **(c)** $Au/Pt/WO_3$; **(d)** Au/WO_3; **(e)** Ni/WO_3; **(f)** Fe/WO_3. Sensors **(a)** to **(c)** were operated at 100 ºC, and sensors **(d)** to **(f)** at 160 ºC.

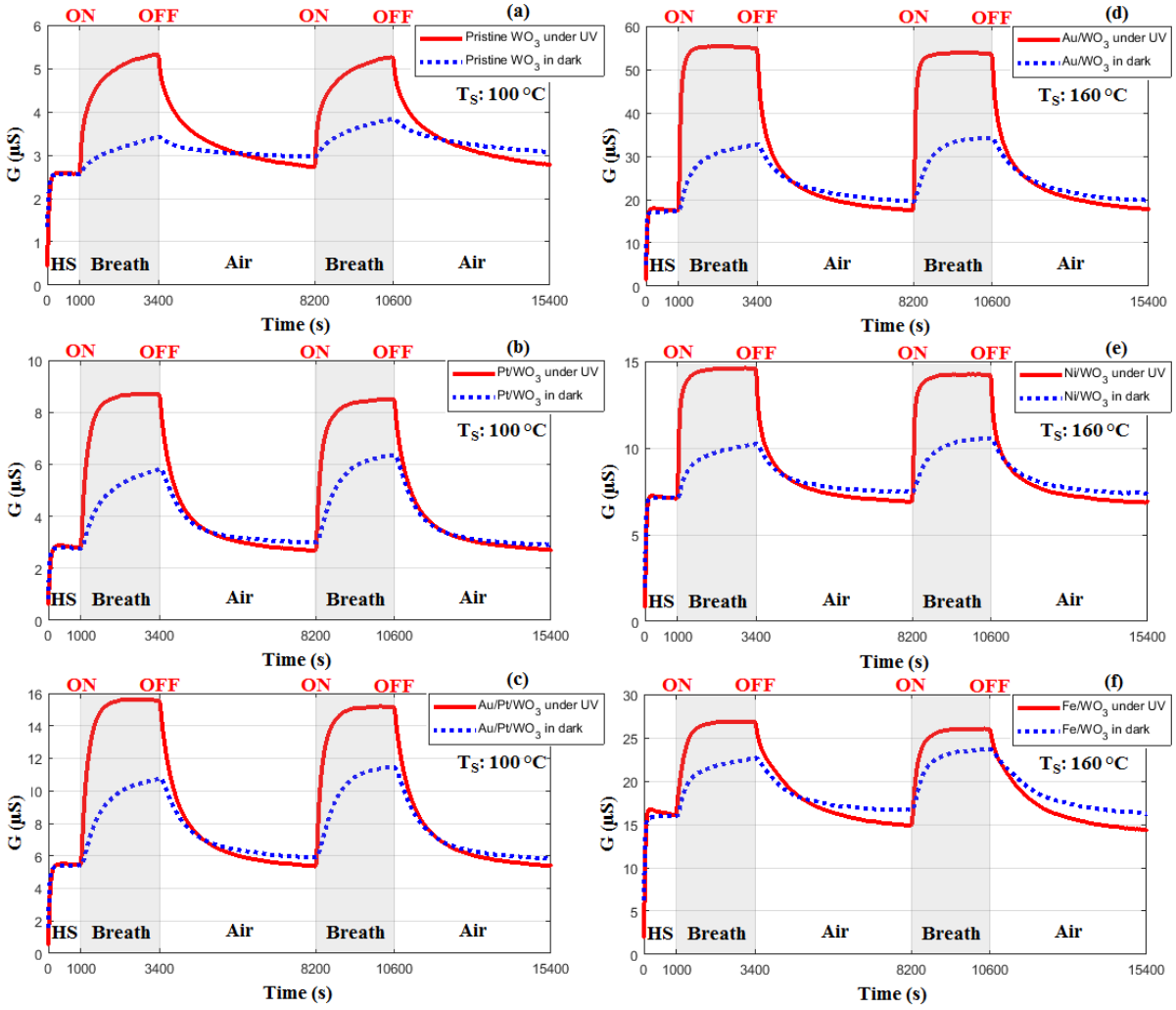

Figure 7 Sensors responses towards two repeated breath exposures in the dark (blue curves) and under UV-light illumination (red curves) for Pristine WO_3 sensor operated at: (a) 90 °C; (b) 110°C; (c) 120 °C; Au/Pt/WO_3 sensor operated at: (d) 90 °C, (e) 110°C; (f) 120 °C; Au/WO_3 sensor operated at: (g) 140 °C; (h) 180 °C; (i) 200 °C.

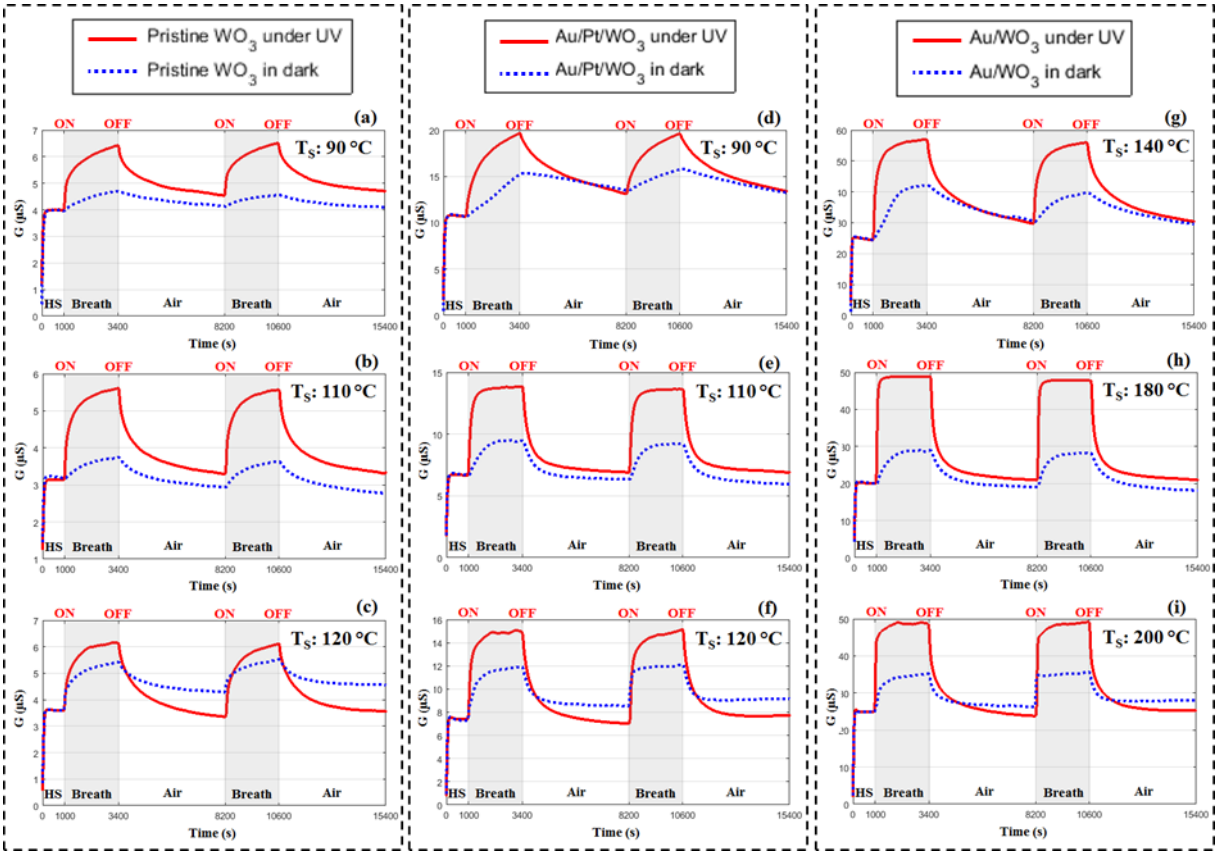

Figure 8 Sensors sensitivities in the presence of breath exposure at four different temperatures for pristine WO_3, Pt/WO_3, $Au/Pt/WO_3$: (a) in dark, (b) under UV irradiation; and Au/WO_3, Ni/WO_3, Fe/WO_3: (c) in dark, (d) under UV irradiation.